Acta Geotechnica (2023) 18:2039–2058
https://doi.org/10.1007/s11440-022-01703-5

RESEARCH PAPER

Effect of rock anisotropy on initiation and propagation of fractures due to fluid pressurization

Yulong Zhang[1] · Jianfu Shao[1,2] · Shu Zhu[1] · Zaobao Liu[3] · Chong Shi[1]

Received: 27 January 2022 / Accepted: 2 September 2022 / Published online: 12 October 2022
© The Author(s), under exclusive licence to Springer-Verlag GmbH Germany, part of Springer Nature 2022

Abstract
The objective of this paper is to study the effect of rock anisotropy on the initiation and propagation of fracture driven by fluid. For this purpose, an improved hydromechanical model considering rock structural anisotropy is established in the framework of the particle flow simulation by assuming that the anisotropic rocks are characterized by a matrix phase with non-persistent weak layers embedded. In this model, the mechanical behavior of rock matrix is described by bond contact while that of weak layers by smooth joint contact, and the fluid flow is reproduced through a new aperture evolution model of pipes redefined according to contact types and orientations. After the calibration of model's parameters, the effectiveness of proposed model is assessed with the help of a typical case of fluid driven fracture around a borehole. The proposed model can successfully describe the local stress anisotropy and fracture reoriented propagation around borehole due to fluid injection. Some additional numerical simulations with different confining stress are also conducted for the typical case. Moreover, a series of sensitive analysis is further realized to investigate effects of inherent rock anisotropy including elastic, strength and permeability on the initiation and propagation of fractures.

Keywords Anisotropic rocks · Discrete element method · Fracture · Hydromechanical model · Particle flow simulation

1 Introduction

Fracture initiation and propagation of rocks driven by fluid are often encountered in underground engineering applications, which is essentially controlled by the coupling interaction between fluid flow and rock deformation [5, 30]. However, due to the existence of oriented fabric elements such as bedding planes and weak layers, most of rocks exhibit inherent anisotropy in terms of hydraulic and mechanical properties [2, 10, 20, 36]. It is very important to consider the influence of rock anisotropy during analysis of hydraulically driven multiple fracture propagation.

For this purpose, large number of experimental hydraulic fracturing studies have been carried out on different kinds of anisotropic rocks. For instance and without giving an exhaustive list of reported studies, Guo et al. [12] have conducted a series of fluid injection tests on shale and found that hydraulic fracture propagation is closely related to the local interaction modes between induced fracture and weak layers. Similar tests have also been performed by Liu et al. [19] on artificial anisotropic rocks and the obtained results show that local fracturing patterns such as crossing, arrested, diverting and dilated behaviors strongly depend on the strength and orientation of weak layers. Tan et al. [28] have further realized true triaxial fluid injection tests on natural shales and investigated the dependence of fracture propagation on weak layers under different confining stresses. Some other studies [22, 44] have even focused on fluid permeability anisotropy induced by orientated weak layers. The geometrical, mechanical and hydraulic properties of weak layers play a crucial role for hydraulic fracturing process in anisotropic rocks.

✉ Jianfu Shao
jian-fu.shao@polytech-lille.fr

1 Key Laboratory of Ministry of Education for Geomechanics and Embankment Engineering, Hohai University, Nanjing 210098, China

2 CNRS, Centrale Lille, UMR9013, LaMcube, University Lille, 59000 Lille, France

3 Key Laborato of Ministry of Education on Safe Mining of Deep Metal Mines, College of Resources and Civil Engineering, Northeastern University, Shenyang 110819, China

In order to describe the fracturing process in anisotropic rocks, different kinds of continuum models have been proposed during the last decades. In general, these models such as the phenomenological models [7, 13] and the micromechanical models [41, 43] describe microcracks initiation and distribution by application of different anisotropic damage criteria. However, it is actually an intractable task to define appropriate criteria to determine the onset condition and propagation direction of fractures of anisotropic rocks. At the same time, due to strong (displacement) discontinuities during localized cracks propagation, different kinds of numerical methods have also been developed, for instance the enriched finite element methods [24], the extended finite element methods [31, 32], the phase-field methods [21] and the discrete element methods [1, 34]. As one of representative discrete element methods, the Particle Flow Code (PFC) has gained more and more attention. In this method, the grain-scale micro-structure of rocks is approximately represented by an assembly of discrete particles and pores [8, 26]. The particles are bonded together. Their overall deformation and failure depends on local behaviors of contacts or bonds. With the help of different contact bond models, it has been successfully applied to failure analysis of anisotropic rocks [25]. More recently, by defining hydraulic pipes at contacts (or bonds), this method is further used to reproduce fluid flow in rocks. Due to the explicit simulation of fluid flow, it can well describe the coupling failure induced by fluid flow and local deformation. Afterward, a great deal of numerical simulations on fluid driven fracture have been carried out, both on isotropic [9, 27, 29], and on anisotropic rocks [6, 29, 35, 42]. Recently, simulations of hydro-fracking in rock mass at meso-scale have been performed by using fully coupled DEM/CFD approach [17]. However, in most of previous studies, a simple model originally embedded in the Particle Flow Code was always used to describe fluid flow in different kinds of anisotropic rocks. In this model, the hydraulic aperture of pipes is isotropically and simplified as a linear function of normal contact force. This definition cannot well describe the aperture evolution with contact force and bond states as well as fluid flow preferential orientation. Moreover, the influences of weak layers geometrical feature are also not taken into account during modeling of cracking process. Therefore, further advances are still required for modeling multi-scale fracturing process in anisotropic rocks.

For this purpose, a new empirical model proposed in our previous study [38] will be used in this research, which defines hydraulic aperture as a nonlinear function of normal force and bond breakage, and can efficiently describe fluid flow in rock matrix and along fractures in isotropic rocks under different stresses. The objective here is to further develop it to describe fluid orientational flow in anisotropic rocks [3, 18]. Based on that, a particle based anisotropic rock sample is first generated by bond- and smooth joint contacts referring to weak layers structural feature. The pipe model between particles is then redefined according to contact (or bond) types. The aperture evolution in pipe model depends on the type and orientation of contact (or bond). Fluid flow in pipes is preferentially oriented. With this model in hand, it shall significantly improve the quantitative description of fluid driven multi-fracture propagation of anisotropic rocks.

This paper is organized as follows. The numerical procedure for the generation of anisotropic rock sample is first presented and then the hydromechanical coupling model describing fluid flow preferential orientation is developed. After the calibration of model's parameters, we assess the effectiveness of the proposed mode by considering a typical case of fluid driven fracture around a borehole. Some additional numerical simulations with different confining stresses are also conducted for the typical case to analyze fracture propagation. A series of sensitive calculations are realized and the results are used to investigate effects of rock anisotropy on the initiation and propagation of fractures.

The following sign convention will be adopted throughout the paper. The compressive normal stress is denoted as a positive value and the tensile normal stress as a negative one. However, the normal opening (aperture) is denoted as positive and the closure as negative.

2 Hydraulic coupling methodology of anisotropic model

In the framework of particle flow simulation, cohesive rocks are represented by an assembly of discrete particles which are connected by bonded interfaces. The macro deformation and failure of rocks are driven by the local behavior of contacts (or bonds). For bond contact model (BM), the neighboring particles are rolling around contact interfaces; for smooth joint contact model (SJM), the neighboring particles are restricted to sliding along the orientated direction. We assume anisotropic rock is represented by an isotropic rock mass with non-persistent weak layers embedded. The isotropic rock mass is composed of a random assembly of particles with bond contacts, while those weak layers are represented by oriented smooth joint contacts.

The numerical procedure to embed smooth joint contacts in isotropic rock matrix is first proposed as illustrated in Fig. 1d. A number of reference contacts are first selected by calculating the differential angle δ between the direction of bond contact (ϕ) and the specified orientation (θ). If the

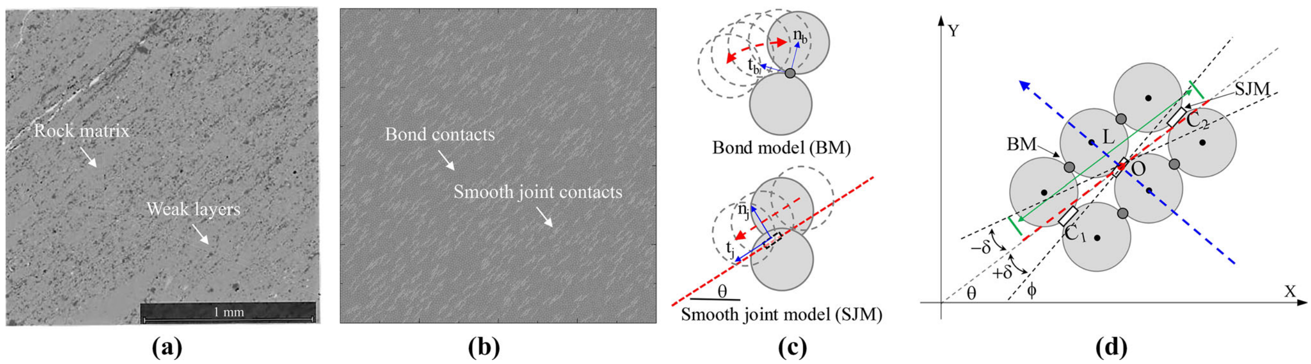

Fig. 1 Illustration of anisotropic rock sample generation: **a** micro-structure scanning image of anisotropic rock [3]); **b** characterization of micro-structure in numerical sample; **c** comparisons of mechanical behavior of particles in two contact models; **d** illustration of choice of smooth joint contacts [25]

differential angle δ meets the tolerance value $\widetilde{\delta}$, the contact between two neighboring particles is then chosen as a reference contact O. Each reference contact is further taken as the center point of a smooth joint zone which is assumed to be a strip shaped with length of L. All bond contacts inside the strip shaped weak layer zone are replaced by smooth joint contacts, such as points of C_1 and C_2 in Fig. 1d. After a series of replacement, the structural anisotropy of rocks can be well reproduced by the particle based model with bond contact and smooth joint contact.

$$\begin{cases} F_n = k_n \mu_n \\ \Delta F_s = -k_s \Delta \mu_s \end{cases} \tag{1}$$

F_n, k_n and u_n are, respectively, the normal force, normal stiffness and displacement at the contact; ΔF_s, k_s and Δu_s denote, respectively, the shear force, shear stiffness and relative displacements in each time step Δt.

$$\begin{cases} k_n = (1 + r_k f(\phi,\theta))k_n^0 & , k_n^0 = 2E_c^0(R_1 + R_2) \\ k_s = (1 + r_k f(\phi,\theta))k_s^0 & , k_s^0 = k_r k_n^0 \\ f(\phi,\theta) = a/(b + (1-b)e^{-c\delta}) - a & , \delta = arctan|\tan(\phi - \theta)| \end{cases} \tag{2}$$

2.1 Anisotropy of elastic stiffness

As mentioned above, in the case of isotropic rocks, the contacts are randomly distributed without preferential orientations. The mechanical behavior of a bond contact is described by an elastic model as Eq. (1). The local elastic stiffness coefficients are the same for all contacts. While in anisotropic rocks, mechanical properties are orientation dependent. The elastic response is depended on the orientation of weak layers. Therefore, inspired by Zhang et al. [40], the local elastic stiffness can be further expanded according to the relative angle (δ) of bond contact direction (ϕ) with respect to weak layer orientation (θ) by Eq. (2), and that:

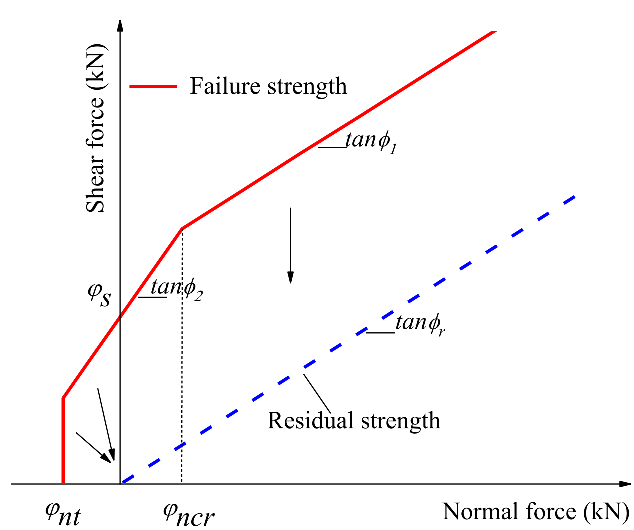

Fig. 2 Peak and residual strength envelopes of bi-linear criterion for two type of contacts [40]

k_n^0 and k_s^0 denote the elastic stiffness of contacts with $\phi = \theta$. The value of k_n^0 is determined from the equivalent elastic modulus E_c^0. R_1 and R_2 are, respectively, the radii of the two neighboring particles. The value of k_s^0 is related to that of k_n^0 by the ratio coefficient k_r, which is related to the macroscopic Poisson's ratio and generally taken as 1.0–3.0. The variable of r_k and function of $f(\phi, \theta)$ are introduced to define the degree of stiffness anisotropy and will be discussed in the Sect. 2.4.

$$F_{s,f} = \begin{cases} 0 & , F_n < \varphi_{nt} \\ \varphi_s + F_n \tan\phi_1 & , \varphi_{nt} \le F_n \le \varphi_{ncr} \\ \varphi_s + \varphi_{ncr}(tan\phi_1 - tan\phi_2) + F_n \tan\phi_2 & , F_n \ge \varphi_{ncr} \end{cases} \quad (3)$$

$$\begin{cases} \varphi_{nt} = (1 + r_s f(\phi, \theta))\varphi_{t0} \\ \varphi_s = (1 + r_s f(\phi, \theta))\varphi_{s0} \\ f(\phi, \theta) = a/(b + (1-b)e^{-c\delta}) - a & , \delta = arctan|\tan(\phi - \theta)| \end{cases} \quad (4)$$

2.2 Anisotropy of mechanical strength

When the local contact force reach the critical values, the bond contact will break according to its strength failure criterion. During this process, two failure modes need to be considered, respectively, the tensile and shear failure, as shown in Fig. 2. Tensile failure occurs when the normal force reaches the critical tensile strength $F_{t,f} = \varphi_{nt}$. The condition for the shear failure is relatively complex due to the fact that the shear strength of contact is strongly dependent on the compressive normal force F_n. In order to better describe this characteristic, a unified mechanical model with bi-linear shear failure criterion for both bond and smooth joint contacts has been proposed in our previous work [39]. This model is still used in the present study. Moreover, accounting for strength anisotropy, the local strength parameters are also redefined similar to the law used in the extension of elastic stiffness by introducing the variable of r_s and function of $f(\phi, \theta)$, and that:

ϕ_1 and ϕ_2 are the frictional coefficients, respectively, for the low and high normal force regime. ϕ_{ncr} denotes the critical transition value of normal force between the two regimes. φ_{t0} and φ_{s0} are the strength parameters for the contacts parallel to weakness layers, i.e., $\phi = \theta$. In addition, for the sake of simplicity, the tensile strength is assumed to disappear completely when bond breakage happens. At the same time, due to roughness of breakage interfaces, the shear strength degrades to a linear function of residual frictional coefficient as $F_{s,r} = F_n \tan\phi_r$.

2.3 Fluid flow behavior

In the particle-based model, the fluid flow occurs through pipes or cracks between particles [38], as illustrated in

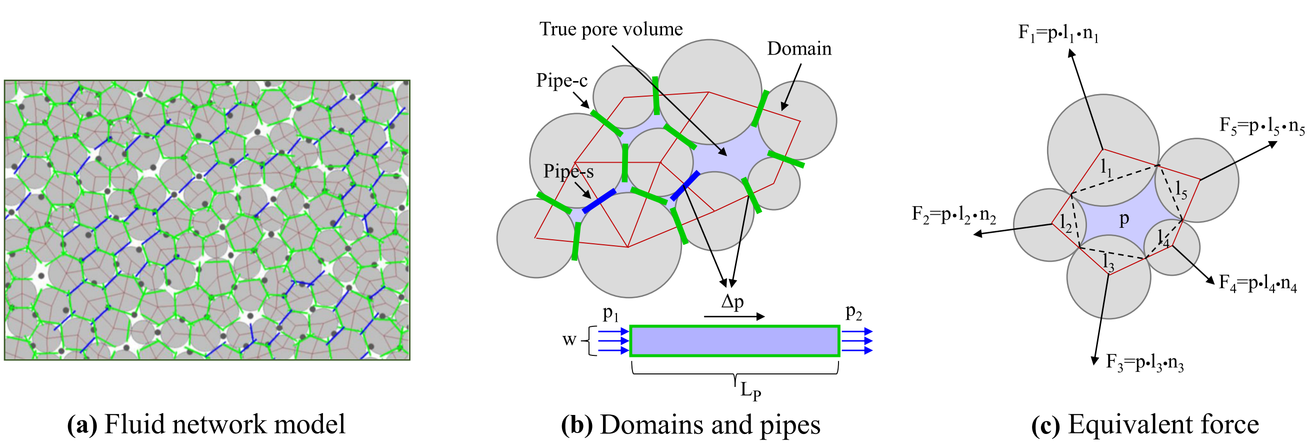

(a) Fluid network model **(b)** Domains and pipes **(c)** Equivalent force

Fig. 3 Fluid flow model considering seepage anisotropy: solid particles (gray circles), two type of flow pipes (green, blue), domains (red polygons) and domain's centers (black points) (color figure online)

Fig. 3. Each pipe is characterized by its aperture and length composed of two hypothetical parallel plates at contacts or bonds. A fictitious domain is created around a pore by connecting the centers of all surrounding particles with red lines. When there is a fluid pressure gradient between two adjacent domains, the driven fluid will flow along pipes to domains. Assuming the out-of-plane thickness is of unit length, the volumetric laminar-flow rate q (m^2/s) in pipes can be expressed by :

$$q = \frac{w^3(p_1 - p_2)}{12\mu L_p} \tag{5}$$

where w and L_p are the hydraulic aperture and length of pipe. μ is the fluid viscosity and $p_1 - p_2$ denotes the pressure difference between adjacent domains. Accordingly, during a time step Δt, the fluid pressure variation inside the domain induced by fluid flow can be calculated as:

$$\Delta p = \frac{K_f}{V_d}\left(\sum q\Delta t - \Delta V_d\right) \tag{6}$$

K_f is the bulk modulus of fluid, V_d and ΔV_d are the domain volume and its variation. After that, the updated fluid pressure induces mechanical deformation of domain by applying the equivalent body force on the surrounding particles. And in turn, the mechanical deformation modifies the aperture of pipes and thus the hydraulic properties. Moreover, the particle displacement induced domain volume change does not directly affect the domain pressure and actually this coupling is one way in the sense of Biot [4, 33]. The detailed coupling of fluid pressure and mechanical deformation is illustrated in Fig. 3c.

During fluid pressure update, the state of bond contact is judged according to its strength failure criterion in each time step Δt. If the bond contact is intact, fluid pressure evolution will obey the relation of Eq. (5). Once bond breakage occurs, the fluid pressure in two adjacent domains will be reallocated equally as $\bar{p} = (p_1 + p_2)/2$. In the subsequent time steps, due to the fluid change between other domains, the values of fluid pressure become again different in two adjacent domain and thus drive fluid flow obeying the law mentioned above.

2.4 Anisotropy of hydraulic aperture

One can find out, the fluid flow in pipes is directly controlled by hydraulic aperture. Therefore, the description of pipe aperture evolution is crucial during mechanical deformation process. Since the common linear model of pipe aperture cannot describe well the dependency of macro permeability on confining stress, an improved empirical model is then proposed in another study of ours [38] to define the evolution of pipe aperture as a nonlinear function of normal force and bond breakage state. The detailed formula is expressed by the first relation of Eq. (7).

On the other hand, in anisotropic rocks, the macro permeability is actually orientation dependent. For the sake of simplicity, we further assume the permeability difference is due to fluid preferential flow along weak layers. In order to describe this inherent feature, a new model of hydraulic pipes is proposed as shown in Figs. 3b and 4a. The hydraulic pipes are redefined according to the types of contacts (or bonds) that include the pipe-c at bond contact and the pipe-s at smooth joint contact, respectively. The aperture parameters of pipe-c is further expanded by using a law similar to anisotropy of mechanical parameters, while these of pipe-s always keep unchanged as largest

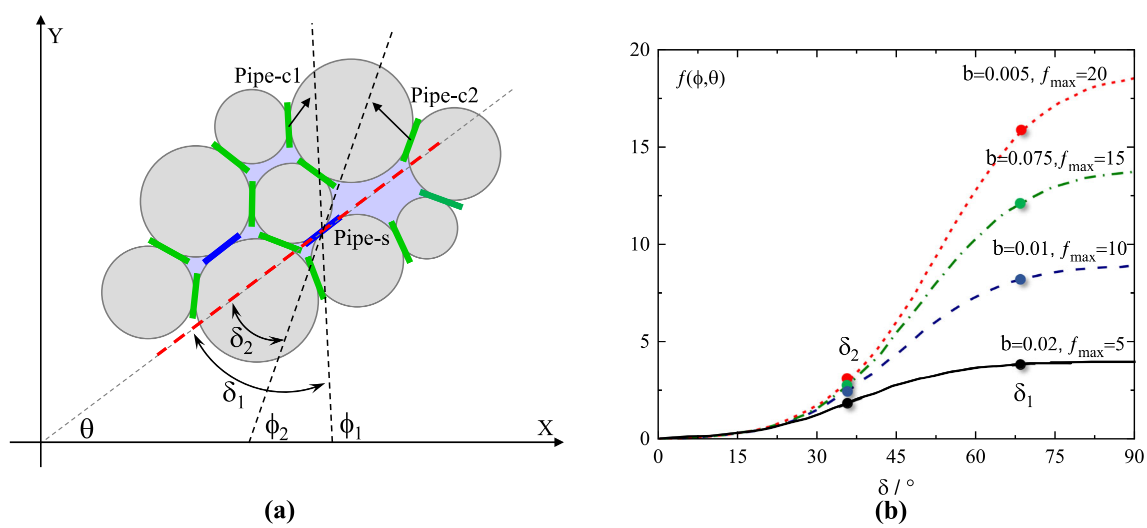

Fig. 4 Calculation of hydraulic aperture of pipes with different orientations: **a** definition of differential angle δ between the direction of ϕ and θ; **b** the function of $f(\phi, \theta), \delta = arctan|\tan(\phi - \theta)|$

values. The improved hydraulic aperture model is expressed by the following relations:

$$w = \begin{cases} w_{res} + (w_{ini} - w_{res})e^{(-\alpha F_n)} & \text{, compressive force} \\ w_{ini} + \beta \Delta d & \text{, tensile force, rupture} \end{cases} \quad (7)$$

$$\begin{cases} w_{ini} = w_0/(1 + r_w f(\phi, \theta)) \\ f(\phi, \theta) = a/(b + (1-b)e^{-c\delta}) - a \end{cases} \quad (8)$$

$$, \delta = arctan|\tan(\phi - \theta)|$$

w_{ini} and w_{res} denote, respectively, the initial and residual aperture of pipes. α, β are aperture evolution parameters. Δd represents the distance between adjacent particles. w_0 denotes the value of hydraulic aperture with $\phi = \theta$, depended on macroscopic permeability.

It should be noted that, the introduced function $f(\phi, \theta)$ is used to define the ratio value of hydraulic aperture for pipes (or mechanical parameters for contacts) with the direction of ϕ and that of θ. Such as shown in Fig. 4b, when the values of a and c take as 0.1, the variation of $f(\phi, \theta)$ with the relative differential angle δ (δ_1, δ_2) is presented for different values of b. The maximum value of $f(\phi, \theta)$ reflects the anisotropy degree of hydraulic aperture (or mechanical parameters) and it is sensitive to the value of b. The maximum value of $f(\phi, \theta)$ is found for $\delta = 90°$, meaning that the minimum aperture value (or maximum mechanical parameters) is achieved for the pipes (or contacts) perpendicular to weak layers. With the help of the function $f(\phi, \theta)$, it is possible to describe macro seepage (or mechanical) property change with weak layer orientation in anisotropic rocks. The values of three parameters a, b and c can be identified from experimental values of fluid flow (or compression) tests performed on anisotropic rock samples with different weak layer orientations.

3 Calibration and assessment of model's parameters

The improved hydromechanical model for different contacts is first implemented in the standard Particle Flow Code (PFC3D4.0). The mechanical and hydraulic parameters involved in this model is then calibrated through numerical simulations of compression and fluid seepage tests.

During this process, the terminology commonly used for rock-like materials are adopted that, the breakage contact is regarded as a tensile micro-crack when the cohesive contact is broken by tensile force, while that as a shear micro-crack by shear force, both in rock matrix and weak layers.

3.1 Generation of anisotropic rock samples

In view of performing numerical simulations, a series of two dimensional samples are first generated. The numerical sample is rectangle of 400 mm in width and 400 mm in hight constituted of about 37,000 uniformly distributed particles. The largest radius of particle is 1.2 mm and the smaller one is 0.8 mm. The choice of particles radius is motivated by the fact that, the particle size effect will largely reduce when the average particle radius is about 40–50 times smaller than the sample size, referred in previous studies [37, 39]. The insertion of parallel smooth joint contacts is conducted according to the algorithm proposed above. Same reason to the choice of particle radius, the tolerance angle $\widetilde{\delta}$ as well as the reference zone L also takes a relative small value so that the thickness of weak layers is also small enough compared to the size of sample. After that, by taking the tolerance angle $\widetilde{\delta}$ of 2.5° and the reference zone L of 5.0 mm, a series of anisotropic rock samples are completed. Seven different orientations of weak layers are considered, ranging from 0° to 90° with a constant interval of 15°. Moreover, four representative samples are presented in Fig. 5.

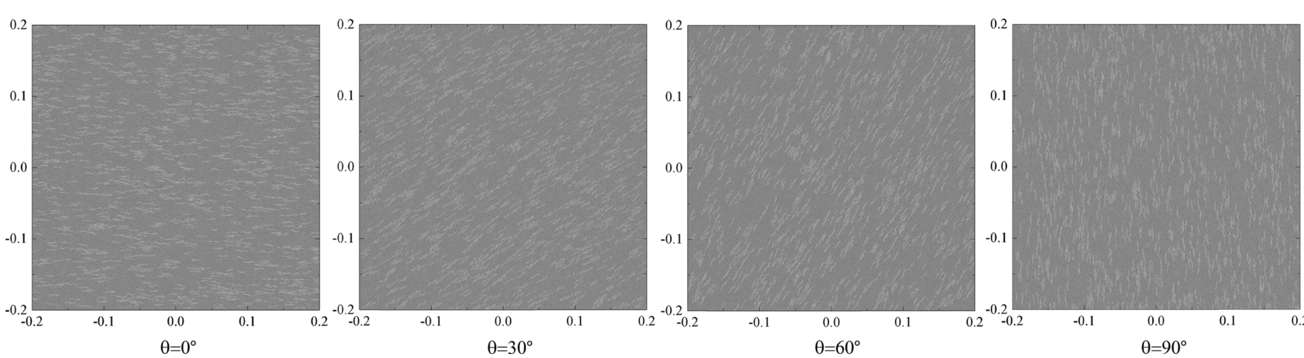

Fig. 5 Four representative anisotropic rock samples

3.2 Calibration of mechanical parameters

In order to describe the mechanical behavior of anisotropic rocks, it is first necessary to identify the elastic and strength parameters for bond and smooth joint contacts from the macroscopic mechanical properties obtained in compression tests by using an iterative procedure. This process can be done through the following two stages referred to our previous study [40].

The first stage mainly identifies the local elastic parameters. To this end, we first set some relative large values for the local strength in both bond and smooth joint contact models to eliminates the possible effect of micro-cracking on elastic response. The initial trial values of k_r and $f_{\max}$ are, respectively, taken as 2.0 and 5.0. And then, the elastic stiffness coefficients of k_n^θ and k_s^θ for contacts with orientation of θ can be obtained by Eq. (2) from the corresponding macro elastic modulus E_c^θ, for instance k_n^0, $k_s^0$and E_c^0 as well as k_n^{90}, $k_s^{90}$and E_c^{90}. After that, by comparing numerical elastic response with experimental results, the value of $f_{\max}$ of $f(\phi,\theta)$ is updated and adjusted. After several iterations, the final local elastic parameters in two bond models can be obtained.

In the second stage, we first fix these identified parameters and the strength parameters in two contact models are then identified from macro failure stresses of two representative orientations of 0° and 45°. For the orientation of 0°, the effect of weak layers on failure is relative small and in this case mainly considers the failure of bond contacts. The strength parameters in two contact models can be set same values and calibrated according to the experimental peak stress of 0°. While for the orientation of 45°, the failure of weak layers gradually becomes a dominant process. In this case, the strength parameters of bond contacts are fixed while that of smooth joint contacts are updated to reproduce the experimental peak stress. And then, the first calibration on strength parameters for both bond and smooth joint contacts is finished. Similarly, the strength parameters can be also determined after several iterations.

Table 1 Geometrical and mechanical parameters used in numerical simulations

Borehole-squared rock sample			
Width of sample (mm)	W		400.0
Height of sample (mm)	H		400.0
Total grain number	N		37000
Average radius (mm)	$\widetilde{R}$		1.0
Diameter of injection borehole (mm)	D		30.0
Mechanical parameters		Bond model	Smooth joint model*
Normal elastic stiffness (N/m)	k_n^0	2.5×10^8	3.0×10^7
Shear elastic stiffness (N/m)	k_s^0	3.7×10^8	4.5×10^7
Friction coefficient for low stress regime	$\tan\phi_2$	1.7	1.5
Friction coefficient for high stress regime	$\tan\phi_1$	0.4	0.3
Tensile failure strength (N)	φ_{t0}	4.2×10^4	2.7×10^4
Shear failure strength (N)	φ_{s0}	1.3×10^5	6.9×10^4
The critical normal force (N)	φ_{ncr}	3.0×10^5	2.0×10^5
Residual friction coefficient	$\tan\phi_r$	0.05	0.05

*These parameters for smooth joint model are calculated with the average radius of contacts between particles

Table 2 Input parameters related to anisotropy response

Parameters used in $f(\phi,\theta)$	Elastic	Strength	Aperture
Variables a, c	0.1, 0.1	0.1, 0.1	0.1, 0.1
Variables $b, f_{\max}$	0.05, 1.89	0.05, 1.89	0.05, 1.89
Variable r_k	1.5	–	–
Variable r_s	–	0.7	–
Variable r_w	–	–	1.0

By following the procedure mentioned above, a series of calibrations are carried out and a set of optimal parameters are given in Tables 1 and 2. The simulated results of anisotropic rock samples with confining pressure of 5 MPa are first given in Fig. 6a–c. One can see that the numerical predictions are in good agreement with experimental results [23], especially for the elastic and strength response. The micro-cracks distribution as well as macro fracture patterns is captured successfully. In addition, a series of uniaxial tension tests are also completed and the obtained peak stress presents an increasing trend with orientation angle (θ). This change is closely related to the failure pattern of anisotropic rock, which is controlled by weak layers under the low orientation angle (θ), but depends on rock matrix for the high one (Fig. 6d).

3.3 Determination of hydraulic parameters

The improved hydrodynamic model mainly has five microscopic parameters needed to be calibrated, respectively, the initial aperture w_0, the anisotropic coefficient r_w, two aperture parameters α and β, and the value of $f(\phi,\theta)$. Among them, the parameters of α and β control pipe aperture evolution and take reference values used in previous studies [38]. The value of $f_{\max}$ keeps consistent as calibrated above. The identification is here primarily on parameters related to the anisotropy as w_0 and r_w.

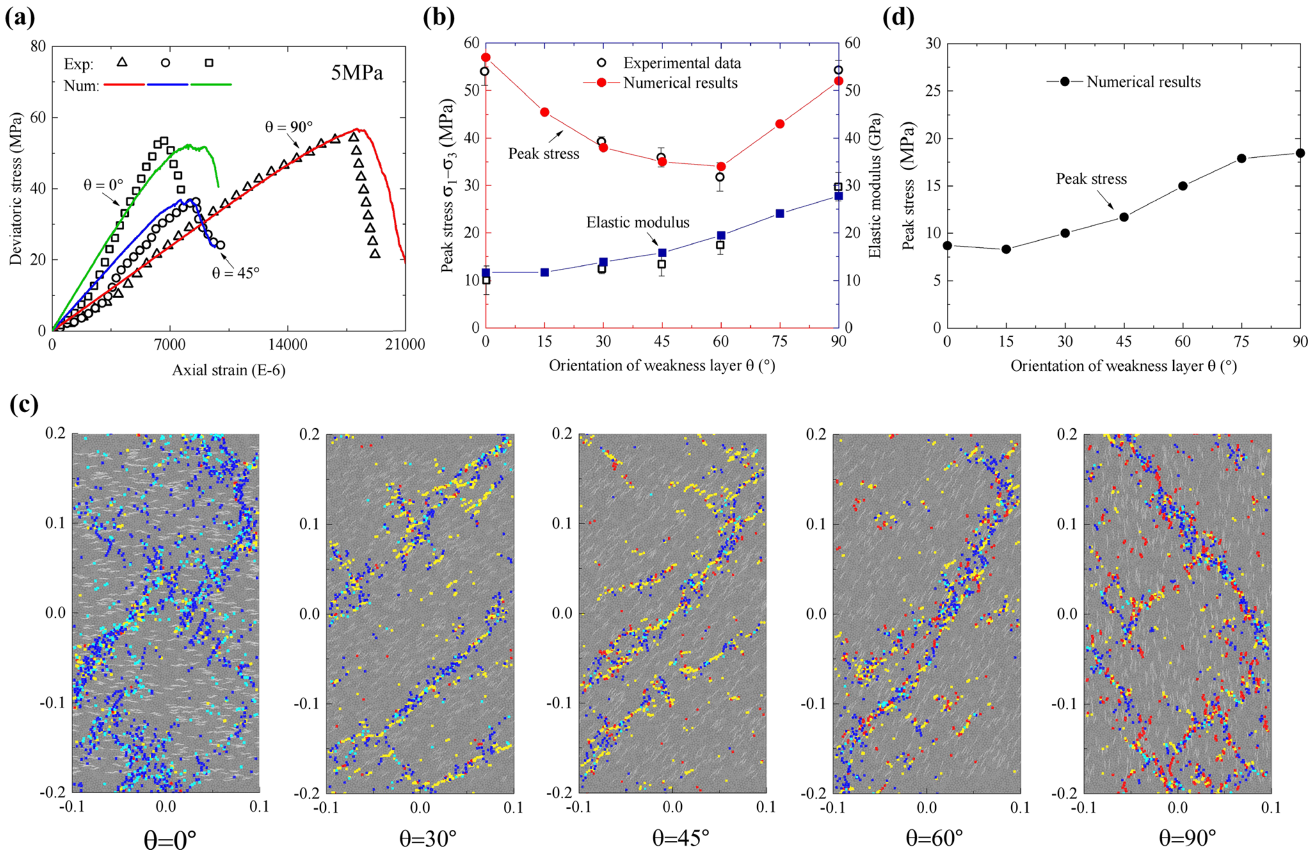

Fig. 6 Results of mechanical parameters calibration: **a** stress-stain curves [23]; **b** comparisons of elastic modulus and peak stress; **c** distribution of micro-cracks of post-failure: blue, cyan represent the tensile, shear cracks in rock matrix; red, yellow denote the tensile, shear cracks in weak layers; **d** peak stresses of tension test (color figure online)

For the first one, the approximation of initial value of w_0 can be obtained with the help of an empirical formula as reported in [42]. But, accounting for fluid pipes anisotropy, its appropriateness should be further adjusted by comparing numerical and experimental permeability in some representative fluid flow tests. For the second one, there is no preferred way to determine that parameter directly from measurable macroscopic data. Inspired by previous studies [27], the value of r_w can be indirectly estimated from the variation of macro permeability with weak layer orientation. Therefore, the numerical fluid flow tests are also necessary. For this purpose, the implementation of fluid flow test is illustrated in Fig. 7a. The improved fluid network considering permeability anisotropy is first introduced into numerical sample and two different fluid pressure of P_{in} = 1 MPa and P_{out} = 0 MPa are applied on the left and right sides. As the steady flow is achieved, the relation of fluid flow rate and pressure gradient can be obtained by the Darcy's law:

$$q_s = \frac{kA}{\mu}\frac{(P_{in} - P_{out})}{W} \tag{9}$$

q_s denotes the steady flow rate per unit area. μ is the fluid viscosity of 7.5 × 10^{-4} Pa.s and $W = 400$ mm is the effective flow length. In general, the steady flow state gets when the inflow and outflow fluid at two sides of rock sample is equal to each other. However, one should note that, depending on the value of permeability, the time needed to reach the steady flow may be faster or shorter. Therefore, the stabilized values of inflow rate is often taken as the steady flow rate [27] and then used for the estimation of average macro permeability k.

A series of fluid flow tests are first performed on anisotropic rock sample with weak layer orientation of 0°. The variation of permeability k with confining stress is shown in Fig. 7d for different hydraulic apertures w_0 and for the coefficient of $r_w = 1.0$. Some empirical relations between permeability and confining stress linked through porosity can be referred [33] to indirectly identify hydraulic aperture w_0. For the sake of simplicity, a more direct way is used here that the value of w_0 can be adjusted and then calibrated by comparing numerical and experimental permeability k. But for the coefficient of r_w, it is hard to be determined by fluid flow tests only considering one kind of

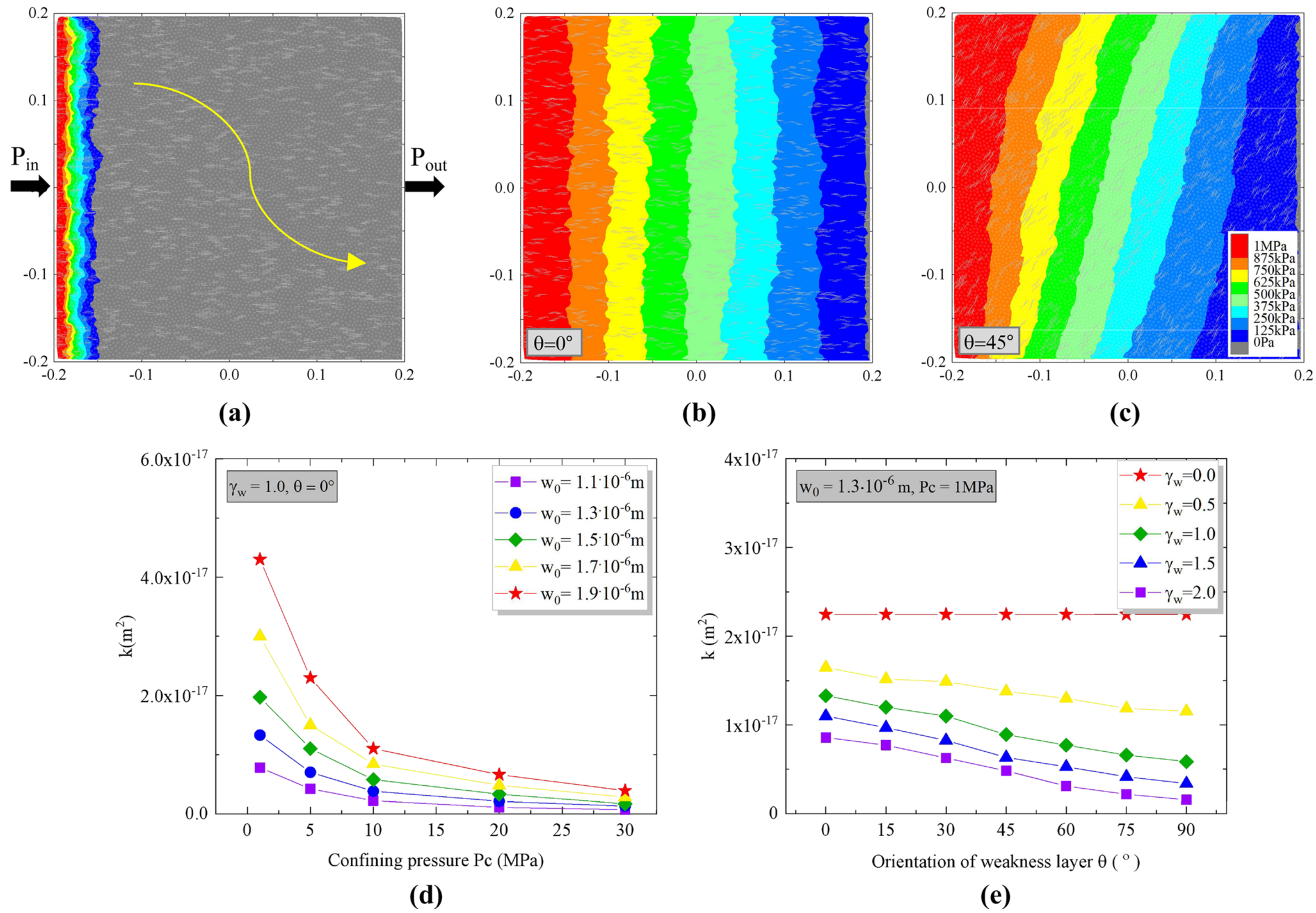

Fig. 7 Results of numerical fluid flow tests: **a** implementation of fluid flow test; **b**, **c** fluid pressure evolution for orientations of 0° and 45°; **d** variation of permeability k to confining stresses (Pc) for different hydraulic apertures w_0; **e** variation of permeability k to weak layer orientations for different anisotropy coefficients r_w

Table 3 Hydraulic parameters used in numerical simulations

Fluid parameters		
Fluid injection rate (m^3/s)		9.0×10^{-6}
Fluid viscosity (pa s)	μ	7.5×10^{-4}
Geometric parameters		
Initial hydraulic aperture (m)	w_0	1.3×10^{-6}
Residual hydraulic aperture (m)	w_{res}	0.13×10^{-6}
Aperture evolution parameters	α, β	2.7×10^{-5}, 0.6
Bulk modulus of fluid (GPa)	K_f	2.0
Macroscopic permeability (m^2)	k	$(1.0–2.0) \times 10^{-17}$

orientated weak layers. Some additional fluid flow tests containing different weak layer orientations are further conducted with confining stresses of 1 MPa. Two representative fluid pressure evolution for orientations of 0° and 45° are given in Fig. 7b, c. The fluid pressure gradient presents obvious orientation dependent. Figure 7e gives the variation of permeability to weak layer orientation for different r_w. It is clear the permeability k gradually decrease with weak layer orientation increase and further that differential value becomes larger with the increase in r_w. According to previous studies, for instance in Refs [44], the differential value measured experimentally is nearly about 1.5–5 times. Here, we take the value as 3.0 and then r_w can be identified to 1.0. Also by several trial and error, a set of optimal parameters are obtained in Tables 2 and 3.

4 Validation and assessment of improved model

In this section, the effectiveness of proposed numerical model is systemically assessed by a classical case of fluid injection on borehole-squared rock sample, in respect of the local stress evolution around borehole and the description of fluid driven fracture propagation.

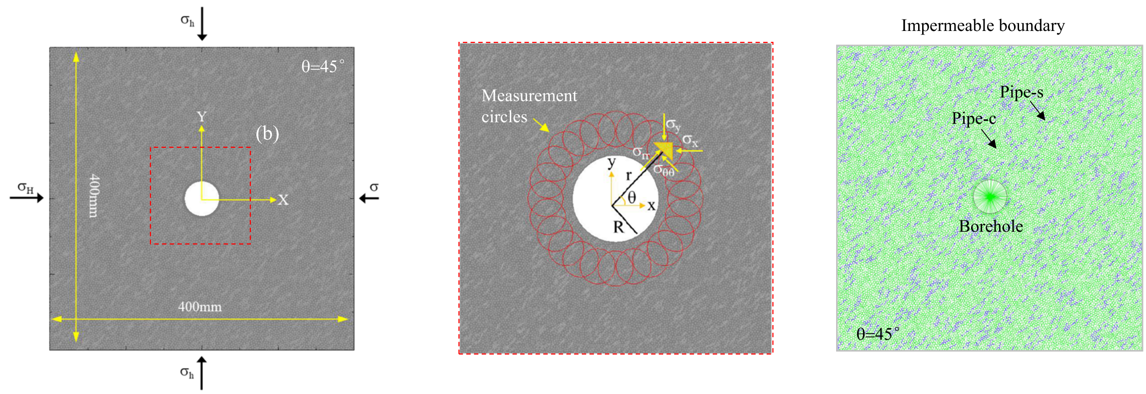

Fig. 8 **a** Set of the numerical sample; **b** placement of the stress measurement circles; **c** fluid flow network

4.1 Setup of loading condition and measurement circles

To this end, a typical borehole-squared sample with 50 mm in diameter used for fluid injection is first completed on the basis of anisotropic rock sample containing weak layers with orientation of 45°. Some well-organized particles with radius of 1.0 mm are placed around the borehole to eliminate effect of material heterogeneity in this zone as best as possible. After the characterization of fluid pipes, a representative rock sample and fluid network model are presented in Fig. 8a, c, respectively. The external boundary of rock sample is four moving walls used to apply the desired confining stress or displacement in both horizontal and vertical directions. Between the boundary and fluid network region, some uncovered particles are remained to represent an impermeable rubber used in actual experiments. In addition, 24 stress measurement circles with radius of 12.5 mm are installed around borehole to record local stress value, such as illustrated in Fig. 8b.

4.2 Assessment of local stress evolution

By adopting the calibrated parameters, a series of fluid injection simulations are performed with two confining stress of 5 and 20 MPa. During this process, the strength parameters are set as large values to avoid borehole breakage. In order to better assess local stress evolution, we consider here three representative cases, respectively, isotropic model (Iso), anisotropic models with (Ani+) and without (Ani−) considering fluid flow anisotropy. Among them, for the case of Iso, the stress distribution around borehole can be calculated by assuming that the borehole fluid does not communicate with the pore in rock matrix, and that [14, 16, 45]:

$$\sigma_{rr} = \frac{\sigma_H + \sigma_h}{2}\left(1 - \frac{R^2}{r^2}\right) + \frac{\sigma_H - \sigma_h}{2}\left(1 - 4\frac{R^2}{r^2} + 3\frac{R^4}{r^4}\right)\cos 2\theta + \Delta p \frac{R^2}{r^2} \tag{10}$$

$$\sigma_{\theta\theta} = \frac{\sigma_H + \sigma_h}{2}\left(1 + \frac{R^2}{r^2}\right) - \frac{\sigma_H - \sigma_h}{2}\left(1 + 3\frac{R^4}{r^4}\right)\cos 2\theta - \Delta p \frac{R^2}{r^2} \tag{11}$$

$$\sigma_{r\theta} = \frac{\sigma_H - \sigma_h}{2}\left(1 + 2\frac{R^2}{r^2} - 3\frac{R^4}{r^4}\right)\sin 2\theta \tag{12}$$

σ_H and σ_h are the maximum and minimum far-field stresses, r is the distance from the interest point to borehole center and R is the borehole radius, ΔP is the fluid injection pressure, here taken the value of 30 MPa.

The numerical results and analytical solutions are compared in Fig. 9a, b. There are always some differences between them, in particular the values of $\sigma_{\theta\theta}$. When confining stress is low, the fluid flow is dominant in all three models and thus $\sigma_{\theta\theta}$ is significantly lower than that calculated analytically. In particular for Ani+ model, since fluid flow is orientation dependent, the variation of $\sigma_{\theta\theta}$ is more pronounced, presenting a wavy stress concentration. When the confining stress becomes large, effect of fluid flow is weaken and the strength of weak layers plays a prominent role. The measured stresses specially for the case of Iso becomes closer to analytical values. The stress values such as $\sigma_{\theta\theta}$ in Ani− and Ani+ models are also closer. Moreover, Fig. 9c shows the fluid pressure distribution around borehole. The pressure contours are more or less circular in the Iso and Ani− models, but appear to be elliptical in the Ani+ model. This suggests that the proposed model is able to capture local stress evolution around the borehole in anisotropic rocks due to weak layers orientation and fluid flow anisotropy.

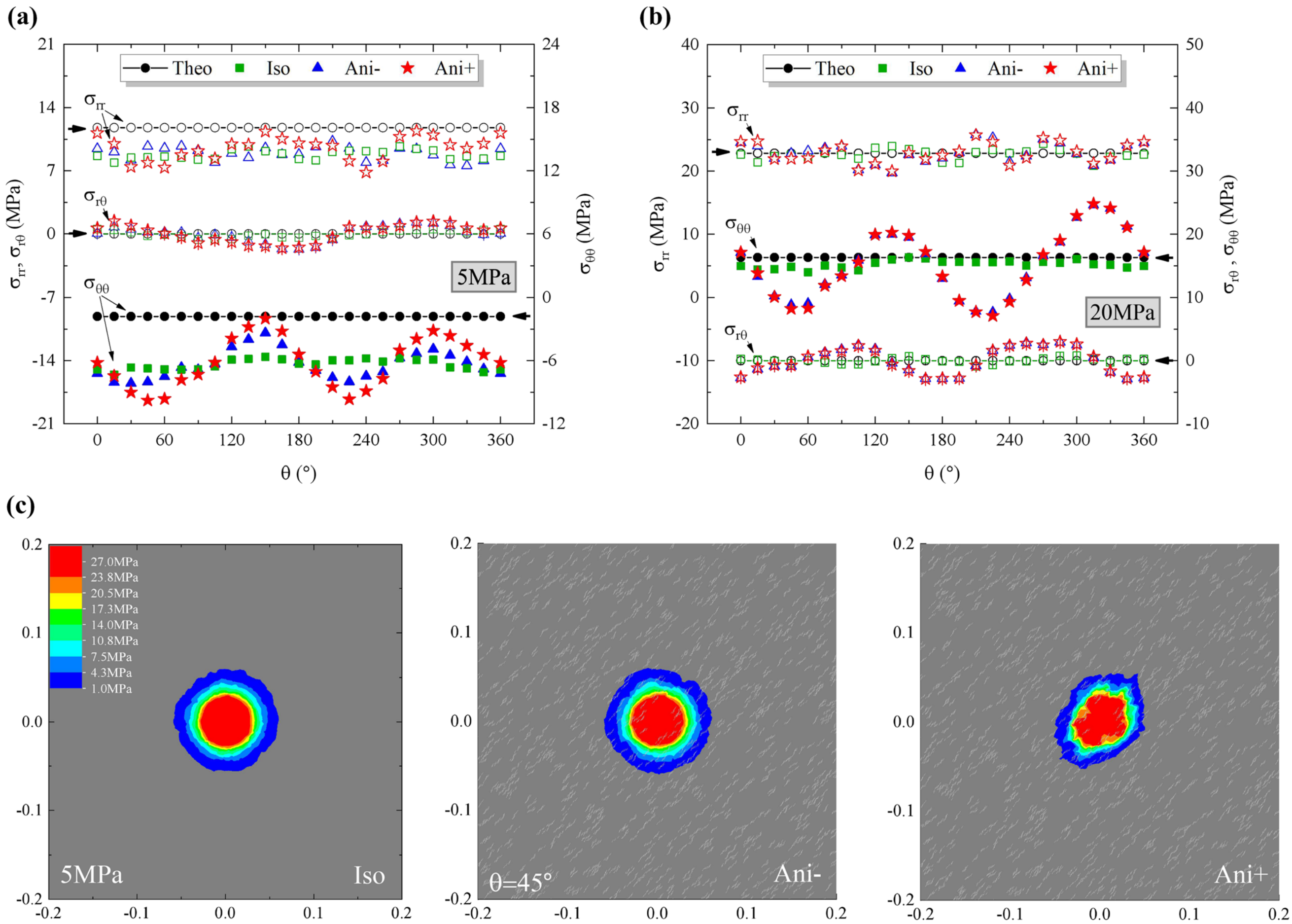

Fig. 9 Comparisons of local stress evolution of three models: **a** 5 MPa; **b** 20 MPa; **c** fluid pressure distribution

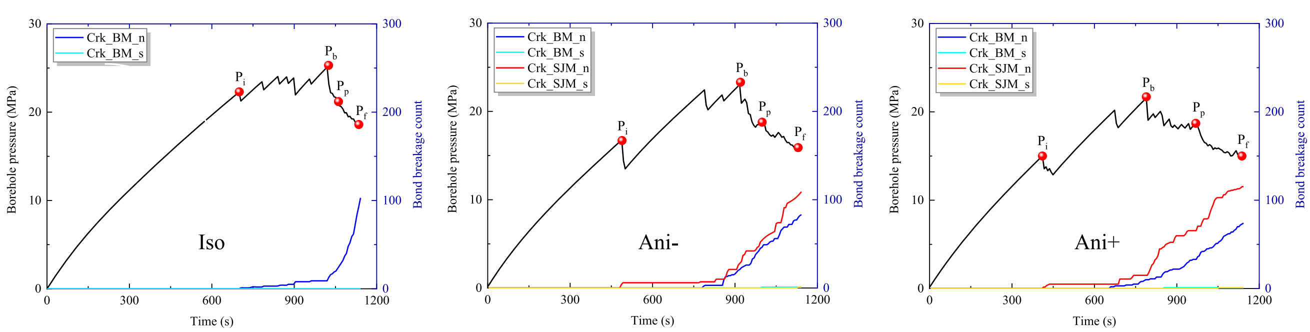

Fig. 10 Curves of borehole pressure and micro-cracks count of three models (5 MPa)

4.3 Comparison of fracture propagation description

In this section, the proposed model is further assessed on the description of fracture propagation with three representative cases mentioned above. The stress of $\sigma_H = \sigma_h =$ 5 MPa is considered and the fluid injection rate is set to 3.0 $\times$ 10^{-6} m^3/s. Other parameters remain as calibrated.

In Fig. 10, we first present the curves of borehole pressure and micro-cracks count of the three models. One can see that, the general trend of borehole pressure of the three models is similar to that observed in experiment [44], which has four remarkable characteristic pressure, respectively, the initial crack pressure p_i, borehole breakdown pressure p_b, fracture propagating pressure p_b and fracture breakthrough pressure p_f. However, by contrast, there are still some differences in the values of characteristic pressure, for instance the p_i and p_b. More precisely, the pressure values of p_i and p_b are decreasing in order for the three models of Iso, Ani− and Ani+. This difference is closely

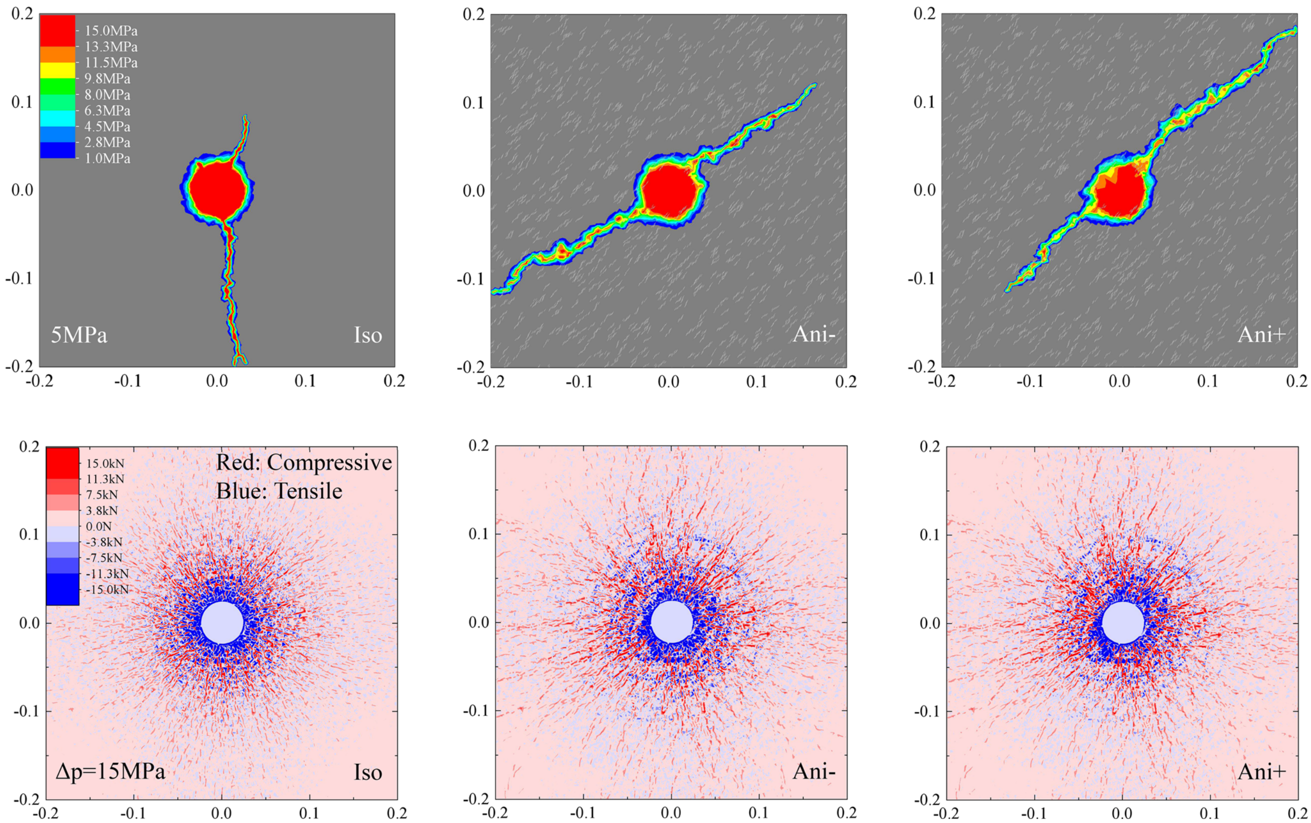

Fig. 11 Fluid pressure evolution along fracture propagation in three models and contact force distribution at the pressure of ΔP = 15 MPa

related to local stress evolution around a borehole as explained above. Overall, the local stress concentration due to weak layers and permeability anisotropy leads to the decrement of borehole pressure response.

The fluid pressure evolution along the hydraulic fracture is shown in Fig. 11. The initial distribution of fluid pressure around the borehole is consistent with that observed in the Sect. 4.2. There are isotropically distributed in Iso and Ani− models, but shows significant orientation dependence in Ani+ model. In particular, we calculate the contact force distribution at the borehole pressure of ΔP = 15 MPa in three models. One can see the tensile force concentration corresponds to fluid pressure evolution. As a consequence, for Iso model, the initial cracking randomly develops around borehole and finally forms a narrow fluid pressure band. While for Ani+ model, the local fracture propagates along weak layers and the preferential fluid flow leads to the formation of a wide fluid pressure zone. Therefore, fluid driven fracture propagation in anisotropic rock is not only controlled by weak layers but also related to fluid flow.

5 Study of fluid driven fracture propagation of anisotropic rocks

In this section, some additional numerical simulations are now conducted with the typical case of Ani+ mentioned above. The objective is to bring a more detailed analysis of hydraulically driven fracturing process in anisotropic rocks with different confining stresses from the aspects of borehole pressure and fracturing patterns.

For this purpose, a series of anisotropic rock samples with a borehole containing different oriented weak layers are generated with a sample size of 400 × 400 mm and borehole diameter of 30 mm. Other parameters and the domain geometry considered are kept the same as those presented above.

5.1 Analysis of fluid injection pressure response

Two representative curves of borehole pressure for rock sample containing weak layers with orientation of 45° are first presented in Fig. 12a, b for confining stresses of 1 and 20 MPa. It is clear that four pressure signatures (p_i, p_b, p_p and p_f) are again captured by the numerical simulations. When the confining stress is of 1 MPa, the pressure has a significant drop stage after borehole breakdown and

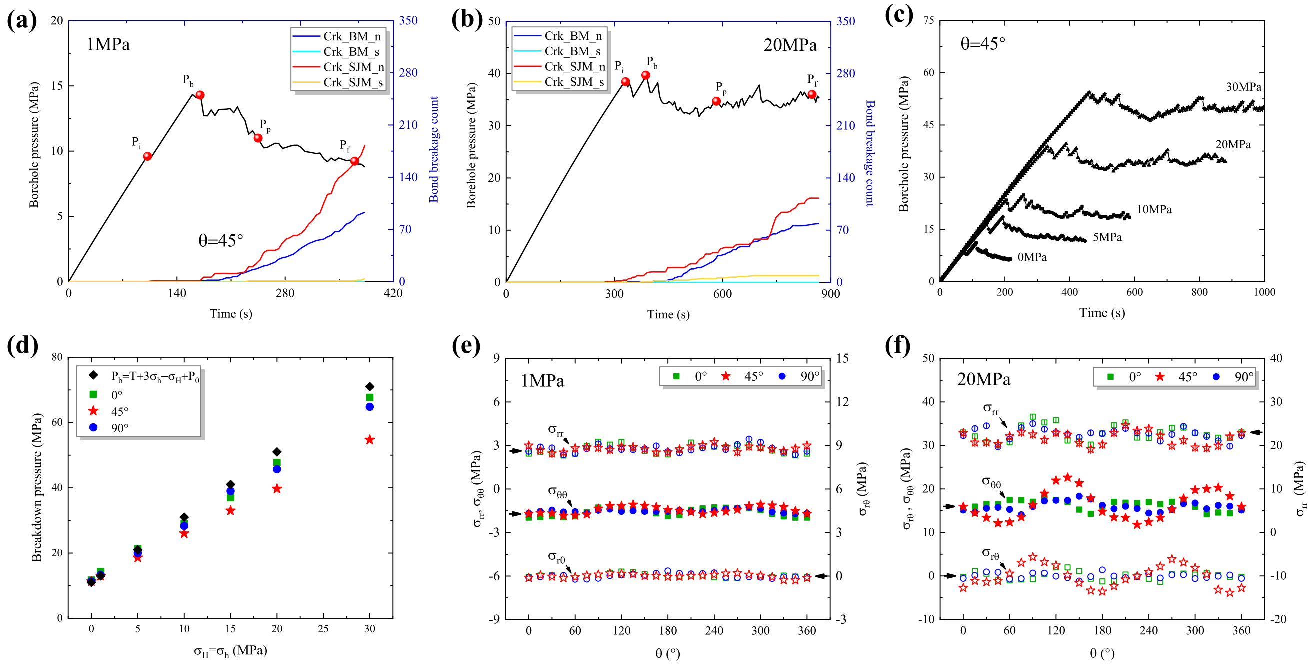

Fig. 12 Variation of borehole pressure response and evolution of local stress around borehole: **a**, **b** two typical curves of borehole pressure for confining stresses of 1 and 20 MPa; **c** variation of borehole pressure to confining stresses for the orientation of 45°; **d** comparisons of numerical and theoretical values of breakdown pressure; **e**, **f** local stress evolution around borehole before breakdown for confining stresses of 1 and 20 MPa

correspondingly micro-cracks increase sharply. The fracturing process exhibits obvious brittleness failure. When the confining stress is 20 MPa, the variation of borehole pressure and micro-cracks becomes gentle. The fracturing failure becomes progressive.

A set of curves of borehole pressure for samples with weak layer orientations of 45° is further given in Fig. 12c for different confining stresses. One can see that the borehole pressure and the time to fracture both have an overall increasing trend. Correspondingly, the fracturing process presents a transition of failure gradually from brittleness to ductile. During this process, the breakdown pressure implies local fracture formation and thus needs to be deserved special attention. In this regard, some analytical solutions can be referred that $P_b = T + 3\sigma_h - \sigma_H - P_0$ [11, 11, 15]. Here, the tensile strength T takes the value of breakdown pressure (10.3 MPa) obtained by fluid injection test without confining stress and the initial pore pressure (P_0) around borehole in rocks is assumed to be 0 MPa. Numerical results and analytical solutions are compared in Fig. 12d. Under low confining stress, there is a good agreement between them. However, with the increase in confining stress, the differential values in breakdown pressure gradually becomes larger, especially for the case of 45°. Therefore, the breakdown pressure response is affected by the combination of weak layer orientation and confining stress.

In order to further investigate this effect, an additional series of simulations are performed on the three representative orientations of 0°, 45° and 90° with confining stresses of 1 and 20 MPa. In the meantime, the local stress around borehole before breakage are measured. Results in Fig. 12e, f show that, the local stress values such as σ_{rr}, $\sigma_{r\theta}$ and $\sigma_{\theta\theta}$ are consistent in all three cases under low confining stress, but gradually become different with confining stress increase. More precisely, for the high confining stress, the tensile (or compressive) stresses of $\sigma_{\theta\theta}$ for orientation of 45° are relatively concentrated and smaller (or larger) than those in other orientations such as 0° and 90°. This local stress concentration leads to the decrement in fluid pressure needed to break borehole. As a result, there forms large differential values in breakdown pressure for the orientation of 0° and 45° as well as 45° and 90°.

5.2 Distribution of micro-cracks and localized fracture

At the same time, Fig. 13 further presents hydraulic fracture propagation as well as micro-cracks distribution of rock samples for that two confining stresses. One can see that regardless of low or high confining stresses, the fracturing process strongly depends on weak layer properties, always propagating along weak layer orientation. However, there are still some differences in micro-cracks

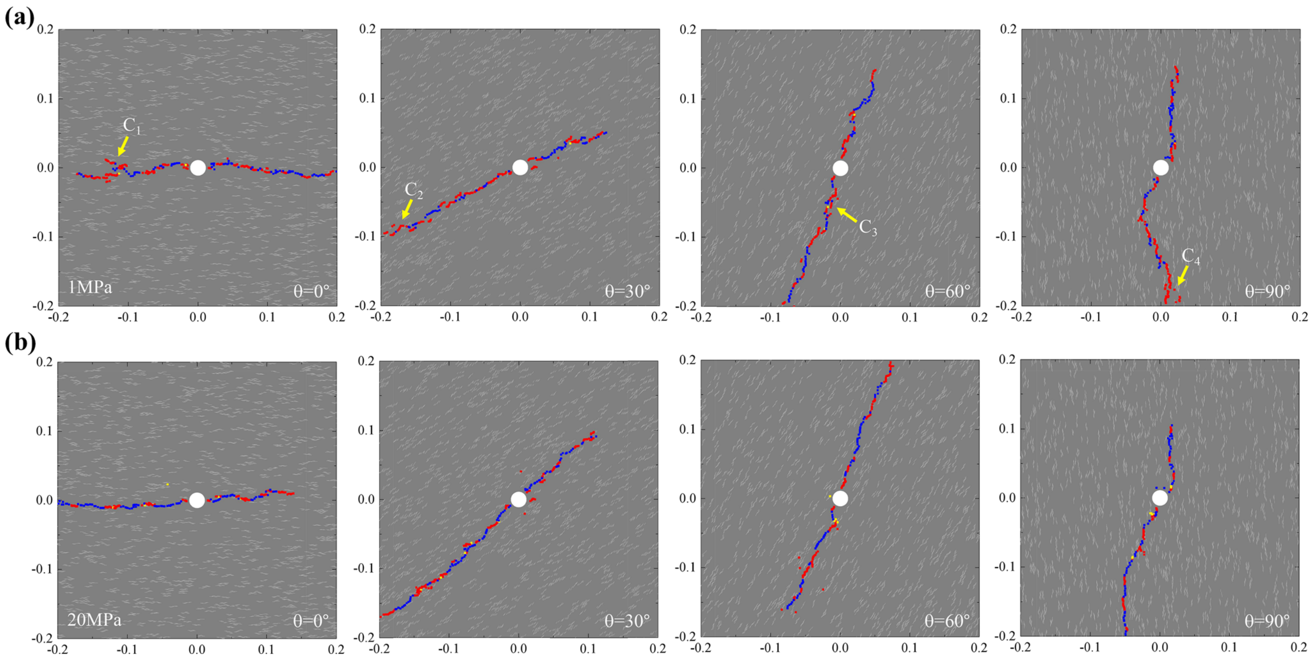

Fig. 13 Fracture propagation patterns of rock samples with different weak layers for two confining stresses: **a** 1 MPa; **b** 20 MPa (color figure online)

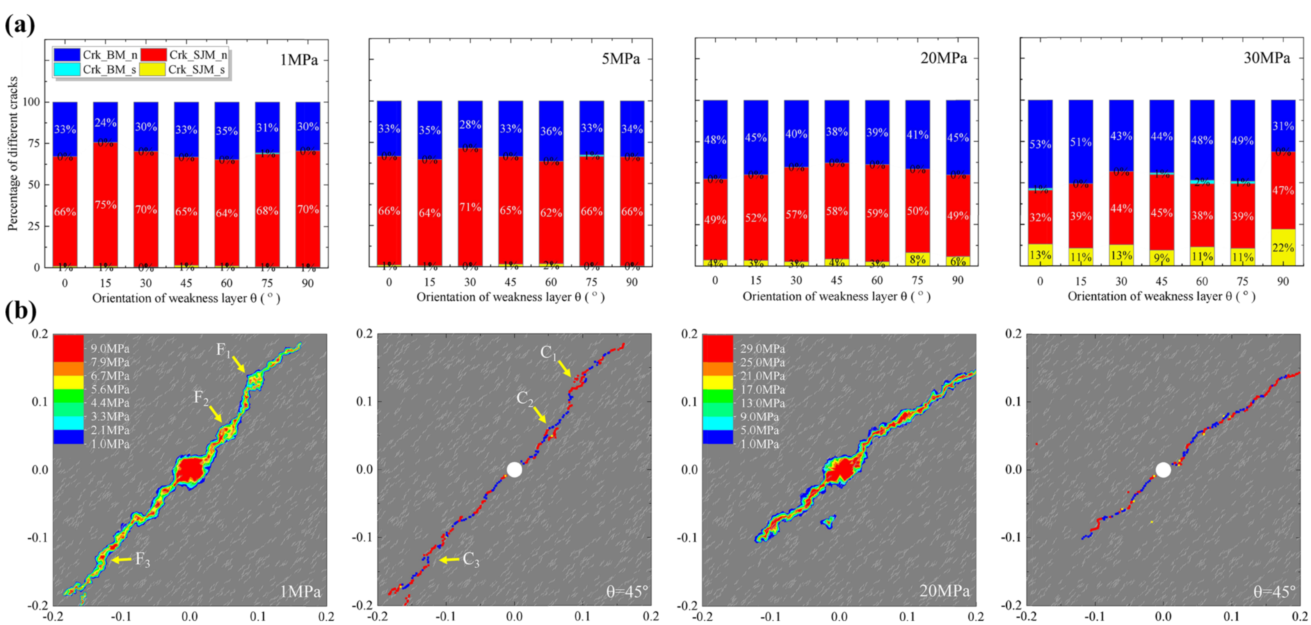

Fig. 14 **a** Variation of micro-cracks ratio to weak layer orientation in rock matrix and weak layers for different confining stresses; **b** fluid pressure and hydraulic fracture distributions for sample containing weak layer with orientation of 45° under confining stresses of 1 and 20 MPa

distributions. Such as shown in Fig. 13a, when confining stress is low, the number of cracks (red ones) along weak layers is significantly larger than that (blue ones) in rock matrix, and thus the failure pattern exhibits obvious brittleness with some bifurcate-shaped cracks formation. Whereas when the confining stress becomes large, the numbers of cracks in both weak layers and rock matrix is similar. The failure process in this case is progressive, forming a relatively smooth fracture.

Further quantitative analysis are provided in Fig. 14a that compares the ratios of micro-cracks in weak layers and rock matrix for seven weak layer orientations and four confining stresses. It is clear the ratios of tensile cracks play a dominant role in both weak layers and rock matrix,

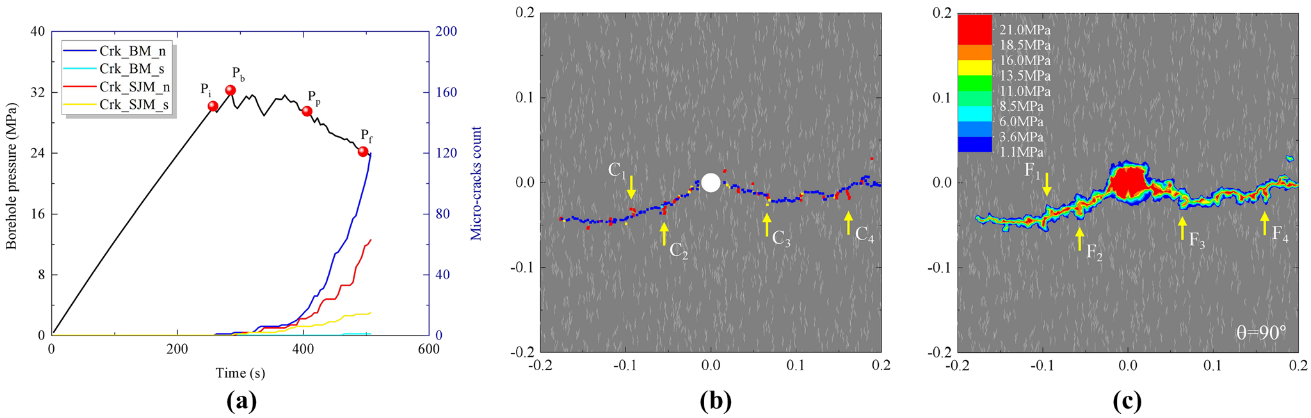

Fig. 15 Numerical results of hydraulically driven fracture with confining stress of σ_H = 10 MPa and σ_h = 5 MPa: **a** borehole pressure with time; **b** fracture propagation pattern; **c** fluid pressure distribution

either for low or high confining stress. For rock matrix, the ratios of tensile cracks (blue ones) in all cases of seven weak layer orientations increase first and then tend to gentle values with confining stress. While for weak layers, the change of crack ratios is relatively complex that is dominated by tensile cracks (red ones) under low confining stress, and by the combined tensile and shear cracks (red and yellow ones) for high confining stress.

In addition, the fracturing process is also related to fluid pressure diffusion. Two representative examples of fluid pressure evolution along hydraulic fracture are presented in Fig. 14b for the orientation of 45°. It is interesting to find that fluid pressure appears a beaded distribution under low confining stress, and a smooth diffusion for high one. This change is mainly due to fluid flow difference. When confining stress is low, the overall permeability of rocks is relatively large, especially in weak layers. It is easily to cause the accumulation of fluid pressure at weak layers during local cracking breakthrough rock matrix. Whereas when confining stress becomes large, due to the permeability smallness in both weak layers and rock matrix, fluid pressure mainly evolutes along hydraulic fracture and finally forms a smooth pressure grade zone.

6 Investigation of rock anisotropy effect on fracture propagation

In this section, the effects of rock anisotropy including elastic, strength and permeability on fracturing process are further investigated and discussed. To this end, a benchmark case of hydraulically driven fracture propagation around a borehole in anisotropic rocks containing weak layers orientation of 90° is here considered with confining stress of σ_H = 10 MPa and σ_h = 5 MPa. Other parameters remain the same as those used above.

The simulated results of benchmark case in Fig. 15a indicate that under the influence of differential stress, the borehole pressure quickly drops after borehole breakdown (p_b) without obvious pressure propagation stage, and accordingly the number of tensile cracks increase sharply in both weak layers and rock matrix. The fracturing pattern shows obvious brittleness characteristic. Moreover, the

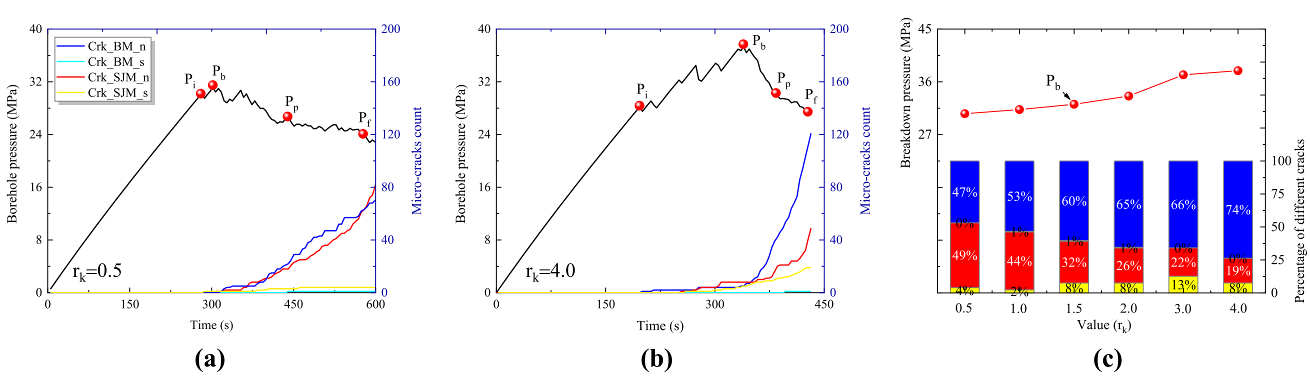

Fig. 16 Numerical results of hydraulically driven fracture with different values of r_k: **a**, **b** two representative cases on curves of borehole pressure and micro-cracks count; **c** variation of breakdown pressure and micro crack ratios to r_k

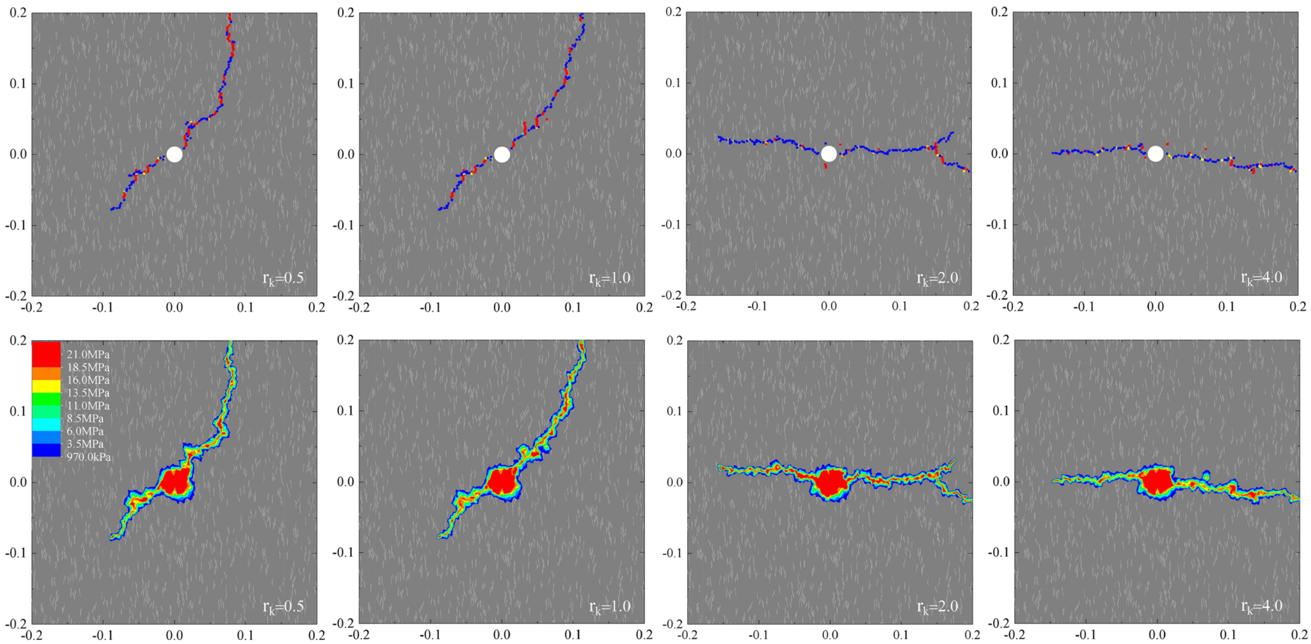

Fig. 17 Hydraulic fracture and fluid pressure distributions under different values of r_k

fracture propagation is re-oriented along the direction of σ_H and meanwhile some longitudinal micro-cracks also develop accompanying with fracture propagation due to the existence of weak layers. As a result, a horizontal fishbone-like fracture as well as fluid pressure evolution band finally forms, as shown in Fig. 15b, c.

6.1 Effect of elastic anisotropy

The local deformation and fracturing process can be influenced by the elastic modulus of rock matrix and weak layers. In order to investigate this effect, a series of additional simulations are carried out on the benchmark case above with the stiffness ratios (r_k) of weak layers to rock matrix increasing from 0.5 to 4.0. Other parameters remain unchanged.

Two representative results on borehole pressure and micro-cracks count are first presented in Fig. 16a, b. It is clear that with the value of r_k increasing from 0.5 to 4.0, the characteristic pressure becomes larger and the time to fracture gets shorter. Micro-cracks in weak layers and rock matrix also change largely that for r_k = 0.5, their number is first close to each other and then dominated by cracks of rock matrix when r_k = 4.0. The local cracking process becomes more and more obvious in brittleness. Further quantitative analysis in Fig. 16c indicates that, the breakdown pressure p_b slightly increases with the value of r_k, and the proportion of tensile cracks in rock matrix gets larger and larger, gradually becoming a dominant factor for fracturing process.

Figure 17 shows the fracturing pattern as well as corresponding fluid pressure evolution for some selected

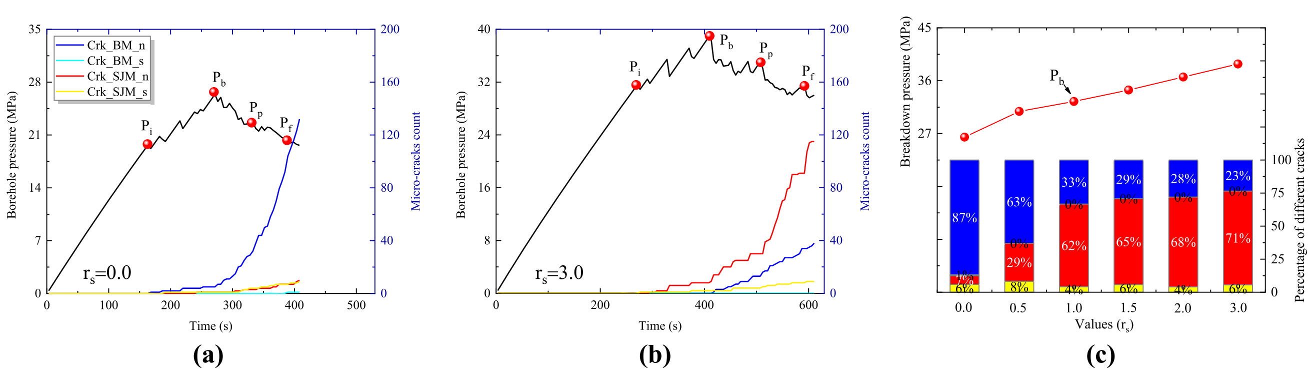

Fig. 18 Numerical results of hydraulically driven fracture with different values of r_s: **a**, **b** two representative cases on curves of borehole pressure and micro-cracks count; **c** variation of breakdown pressure and micro-crack ratios to r_s

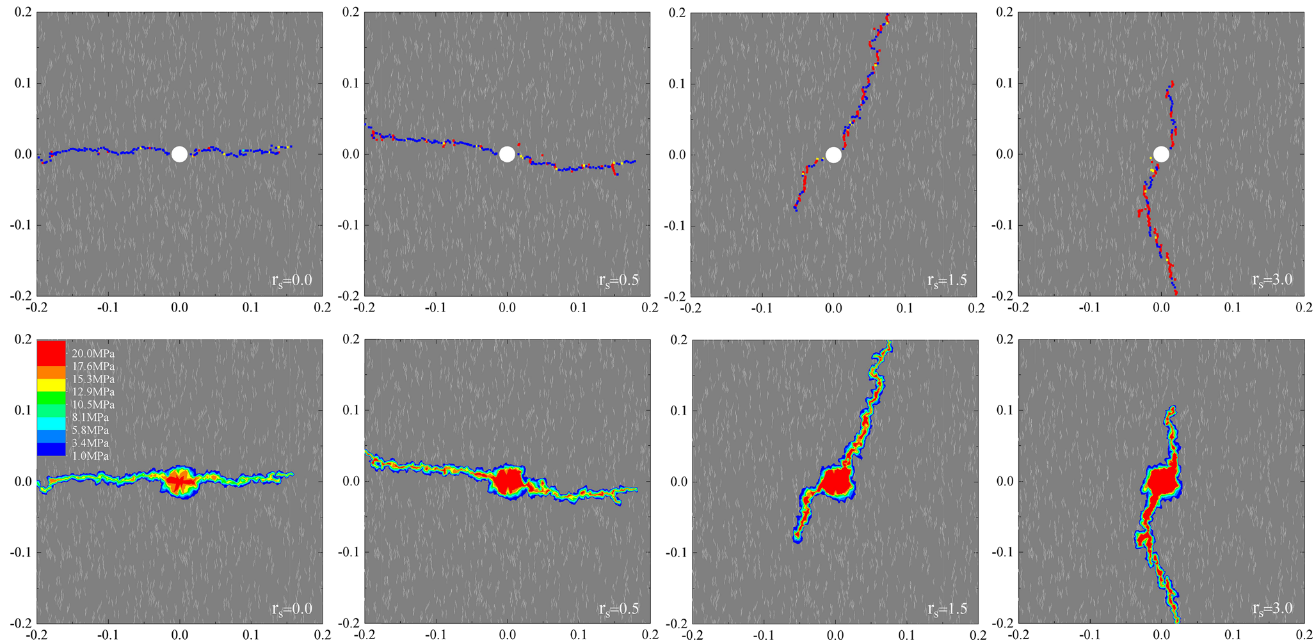

Fig. 19 Hydraulic fracture and fluid pressure distributions under different values of r_s

values of r_k including 0.5, 1.0, 2.0 and 4.0. It is seen that with the increase in r_k, the fracture propagation is first along the vertical direction depended on weak layers and then along the horizontal direction controlled by the maximum stress. Moreover, the T-shaped fracturing pattern often observed in experiments [18] is also captured successfully by the case of $r_k = 2.0$. The enhancement in elastic of rock matrix with respect to weak layers makes rock matrix more prone to local cracking. However, due to the strength and permeability unchanged, the increase in breakdown pressure p_b is limited and accordingly fluid pressure presents similar evolution along fracture propagation.

6.2 Effect of strength anisotropy

In this section, the effects of strength anisotropy on fracturing process are investigated. For this purpose, a series of simulations are performed on the benchmark case by increasing the strength ratios r_s from 0.0 to 4.0. Other parameters remain unchanged.

Also two representative results on borehole pressure and micro-cracks count are compared in Fig. 18a, b. When the value of $r_s = 0.0$, the breakdown pressure p_b is small and the time to fracture is short. Whereas when the value of $r_s = 3.0$, the breakdown pressure p_b and the time to fracture both increase. The fracturing process presents a transition from brittleness to ductile. As can be seen from Fig. 18c, the breakdown pressure p_b has an obvious increasing trend with the strength ratio r_s. At a low value of

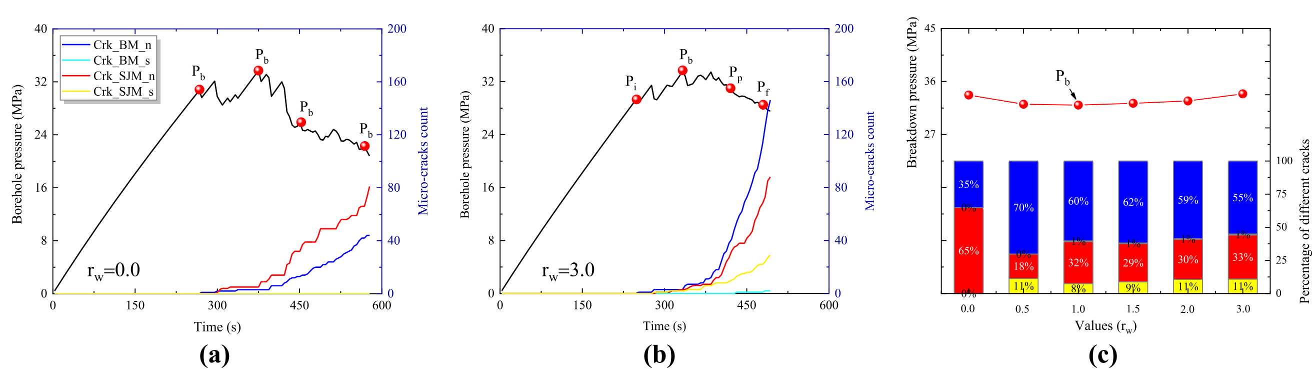

Fig. 20 Numerical results of hydraulically driven fracture with different values of r_w: **a**, **b** two representative cases on curves of borehole pressure and micro-cracks count; **c** variation of breakdown pressure and micro-crack ratios to r_w

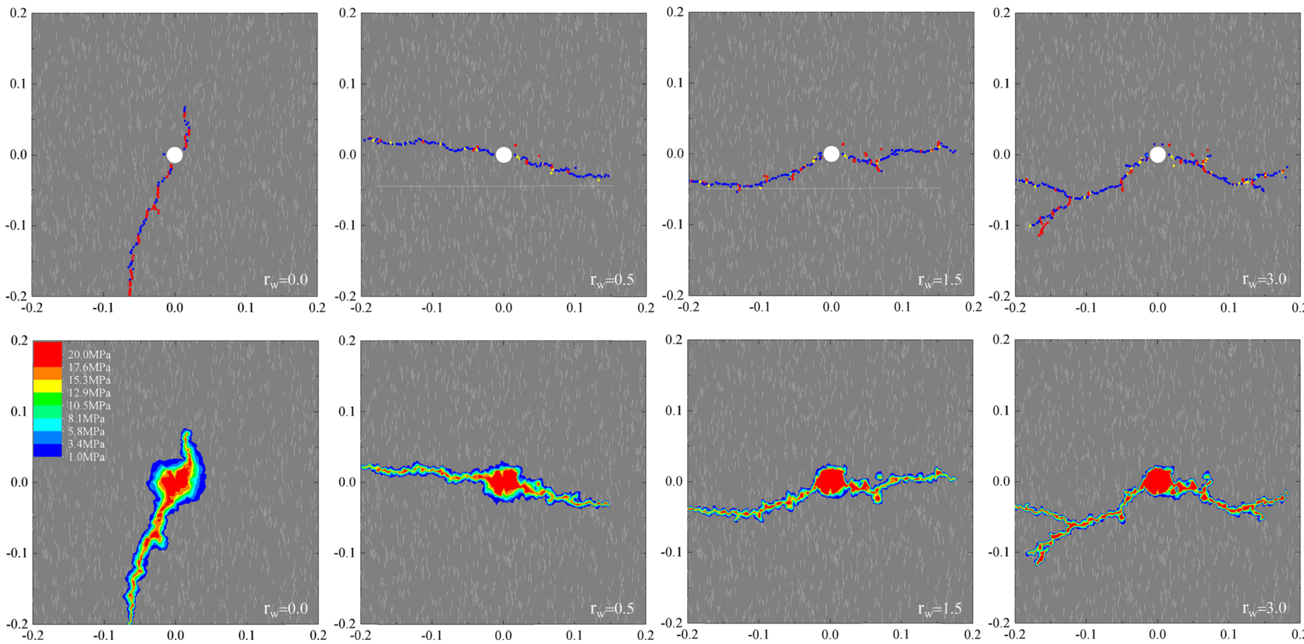

Fig. 21 Hydraulic fracture and fluid pressure distributions under different values of r_w

r_s, the ratio of tensile cracks in rock matrix is larger than that in weak layers, while for the high one, their ratios are completely opposite.

In consistent to the variation of micro-cracks ratios, the fracture propagation is also reoriented from horizontal to vertical direction increasing with the strength ratio r_s, as shown in Fig. 19. More precisely, for a low ratio such as 0.0, rock strength is almost isotropically and in this case local cracking is controlled by the maximum stress. While for a high one, the strength of rock matrix with respect to weak layer becomes large and local cracking is forced to propagate along weak layers. Some extra fluid pressurization are required to maintain fracture propagation. Therefore, fluid pressure around borehole and along fracture both increase, changing from light orange to dark red color.

6.3 Effect of permeability anisotropy

Permeability anisotropy affects the kinetics of fluid flow and accordingly the fracturing process. In this section, the effects of permeability anisotropy on fluid pressure evolution and fracturing pattern are investigated. For this purpose, a series of hydraulically-driven fracture simulations are conducted with the coefficient of permeability anisotropy r_w increasing from 0.0 to 3.0.

Again two representative results on borehole pressure and micro-cracks count are given in Fig. 20**a**, **b**. One can see that in two cases of $r_w = 0.0$ and $r_w = 3.0$, the breakdown pressure p_b seems to be consistent, but the number of micro-cracks is different. In particular, when the value of r_w is equal to 3.0, the number of tensile cracks in rock matrix increase sharply and the time to fracture propagation is shorten obviously. The local cracking process is prone to brittle failure. This trend is also certified by the variation of micro-cracks proportions presented in Fig. 20c. However, the breakdown pressure p_b does not appear to be significantly affected.

In addition, the fracturing patterns and corresponding fluid pressure evolution in Fig. 21 show that in the case of $r_w = 0$, the fluid flow is isotropically with largest value in any orientation and local fracture propagates along weak layers. With the increase in r_w, the fluid flow gradually appears anisotropy and then local fracture is reoriented along the horizontal direction. In particular, when $r_w = 3.0$, the fluid is almost impermeable in rock matrix and only flows along weak layers. In this case, local cracking both occurs in horizontal direction and weak layers, and finally forms a complex fracture with some branch cracks. Moreover, due to permeability anisotropy, the fluid pressure evolution around borehole and along fracture also changes largely that forms a wide pressure diffusion zone for $r_w = 0$, but a narrow concentrated band for $r_w = 3.0$.

7 Conclusions

In this paper, we have developed a new particle-based hydromechanical coupled model suitable for modeling hydraulic fracture propagation of anisotropic rocks. This model can well take into account the anisotropy of rock deformation and fluid flow by reconfiguring different kinds of bond contacts and by redefining different evolution laws of pipe apertures.

The effectiveness of the proposed model has been assessed with the help of a typical case of hydraulically driven fracture around a borehole. It is clear that the new proposed model can successfully capture the local stress anisotropy and the oriented fracturing process around a borehole due to fluid injection. An additional series of numerical simulations for this typical case with different confining stresses indicate that, the fracture propagation presents a strong dependence on weak layers and fluid flow. The local cracking of rock matrix and weak layers is dominated by the tension cracks regardless of small or large confining stress, and the failure patterns have a transition from brittleness to ductile with confining stress increase.

In addition, a series of anisotropic parameter sensitivity studies have also been carried out. The obtained results suggest that, both the borehole pressure and fracturing patterns are influenced by the anisotropy of elastic properties, strength and permeability. More precisely, the increase in elastic modulus of rock matrix with respect to weak layers makes local cracking more likely to occur in rock matrix, but has a limited promotion for borehole pressure. The strength enhancement in rock matrix forces the fracture reorientation to propagate along weak layers, and thus leads to an obvious increase in borehole pressure. The variation of permeability seems to have little effect on borehole pressure, but makes the fracturing patterns become more complex.

The time-dependent creep deformation of rock can pay an important role in long term fracturing process and should be investigated in our future studies.

Acknowledgments This study has been jointly supported by the State Key RD Program of China (Grant No. 2017YFC1501100), China Postdoctoral Science Foundation (Grant No. 2019TQ0080, Grant No. 2020M671320), and the Key Laboratory of Ministry of Education on Safe Mining of Deep Metal Mines (Grant No. DM2019K02).

References

1. Al-Busaidi A, Hazzard J, Young R (2005) Distinct element modeling of hydraulically fractured lac du bonnet granite. J Geophys Res: Solid Earth 110:B06302
2. Amadei B (1996) Importance of anisotropy when estimating and measuring in situ stresses in rock. Int J Rock Mech Min Sci 33:293–325
3. Ambrose J, Zimmerman R, Suarez-Rivera R (2014) Failure of shales under triaxial compressive stress. In: The 48th U.S. rock mechanics/geomechanics symposium. American Rock Mechanics Association
4. Biot MA (1941) General theory of three-dimensional consolidation. J Appl Phys 12:155–164
5. Bybee K (2009) Proper evaluation of shale-gas reservoirs leads to more-effective hydraulic-fracture stimulation. J Pet Technol 61:59–61
6. Chong Z, Karekal S, Li X, Hou P, Yang G, Liang S (2017) Numerical investigation of hydraulic fracturing in transversely isotropic shale reservoirs based on the discrete element method. J Nat Gas Sci Eng 46:398–420
7. Cormery F, Welemane H (2007) A critical review of some damage models with unilateral effect. Mech Res Commun 29:391–395
8. Cundall PA, Strack ODL (1979) A discrete numerical model for granual assemblies. Geotechnique 29:47–65
9. Duan K, Kwok CY, Wu W, Jing L (2018) Dem modeling of hydraulic fracturing in permeable rock: influence of viscosity, injection rate and in situ states. Acta Geotech 13:1187–1202
10. Fjær E, Nes OM (2014) The impact of heterogeneity on the anisotropic strength of an outcrop shale. Rock Mech Rock Eng 47:1603–1611
11. Gan Q, Elsworth D, Alpern J, Marone C, Connolly P (2015) Breakdown pressures due to infiltration and exclusion in finite length boreholes. J Pet Sci Eng 127:329–337
12. Guo T, Zhang S, Qu Z, Zhou T, Xiao Y, Gao J (2014) Experimental study of hydraulic fracturing for shale by stimulated reservoir volume. Fuel 128:373–380
13. Haddag B, Abed-Meraim F, Balan T (2009) Strain localization analysis using a large deformation anisotropic elastic-plastic model coupled with damage. Int J Plast 25:1970–1996
14. Haimson B (2007) Micromechanisms of borehole instability leading to breakouts in rocks. Int J Rock Mech Min Sci 44:157–173
15. Haimson B, Fairhurst C, Fairhurst C (1967) Initiation and extension of hydraulic fractures in rocks. Soc Pet Eng J 7:310–318
16. Kirsch C (1898) Die theorie der elastizitat und die bedurfnisse der festigkeitslehre. Ztschr Vernes Deutsch Ing 42:797–807
17. Krzaczek M, Nitka M, Kozicki J, Tejchman J (2020) Simulations of hydro-fracking in rock mass at meso-scale using fully coupled DEM/CFD approach. Acta Geotech 15:297–324
18. Li Z, Li L, Li M, Zhang L, Tang C (2017) A numerical investigation on the effects of rock brittleness on the hydraulic fractures in the shale reservoir. J Nat Gas Sci Eng 50:22–32
19. Liu Z, Chen M, Zhang G (2014) Analysis of the influence of a natural fracture network on hydraulic fracture propagation in carbonate formations. Rock Mech Rock Eng 47:575–587
20. Meier T, Rybacki E, Reinicke A, Dresen G (2013) Influence of borehole diameter on the formation of borehole breakouts in black shale. Int J Rock Mech Min Sci 62:74–85
21. Miehe C, Schaenzel LM, Ulmer H (2015) Phase field modeling of fracture in multi-physics problems. Part I. Balance of crack surface and failure criteria for brittle crack propagation in thermo-elastic solids. Comput Methods Appl Mech Eng 294:449–485
22. Moghaddam RN, Jamiolahmady M (2016) Fluid transport in shale gas reservoirs: simultaneous effects of stress and slippage on matrix permeability. Int J Coal Geol 163:87–99
23. Niandou H, Shao J, Henry J, Fourmaintraux D (1997) Laboratory investigation of the mechanical behaviour of tournemire shale. Int J Rock Mech Min Sci 34:3–16
24. Oliver J (1996) Modelling strong discontinuities in solid mechanics via strain softening constitutive equations, part 1: fundamentales. Int J Numer Methods Eng 39:3575–3600
25. Park B, Min KB (2015) Bonded-particle discrete element modeling of mechanical behavior of transversely isotropic rock. Int J Rock Mech Min Sci 76:243–255
26. Potyondy ADO, Cundall BPA (2004) A bonded-particle model for rock. Int J Rock Mech Min Sci 41:1329–1364

27. Shimizu H, Murata S, Ishida T (2011) The distinct element analysis for hydraulic fracturing in hard rock considering fluid viscosity and particle size distribution. Int J Rock Mech Min Sci 48:712–727
28. Tan P, Jin Y, Han K, Hou B, Chen M, Guo X, Gao J (2017) Analysis of hydraulic fracture initiation and vertical propagation behavior in laminated shale formation. Fuel 206:482–493
29. Wang T, Zhou W, Chen J, Xiao X, Li Y, Zhao X (2014) Simulation of hydraulic fracturing using particle flow method and application in a coal mine. Int J Coal Geol 121:1–13
30. Warpinski NR, Mayerhofer MJ, Vincent MC, Cipolla CL, Lolon EP (2009) Stimulating unconventional reservoirs: Maximizing network growth while optimizing fracture conductivity. J Can Pet Technol 48:39–51
31. Zeng QD, Yao J, Shao JF (2018) Numerical study of hydraulic fracture propagation accounting for rock anisotropy. J Pet Sci Eng 160:422–432
32. Zeng QD, Yao J, Shao JF (2019) Study of hydraulic fracturing in an anisotropic poroelastic medium via a hybrid EDFM-XFEM approach. Comput Geotech 105:51–68
33. Zhang F, Damjanac B, Huang H (2013) Coupled discrete element modeling of fluid injection into dense granular media. J Geophys Res: Solid Earth 118:2703–2722
34. Zhang F, Wang T, Liu F, Peng M, Bate B, Wang P (2022) Hydro-mechanical coupled analysis of near-wellbore fines migration from unconsolidated reservoirs. Acta Geotech 17:3535–3551
35. Zhang Q, Zhang XP, Sun W (2020) Hydraulic fracturing in transversely isotropic tight sandstone reservoirs: a numerical study based on bonded-particle model approach. J Struct Geol 136:104068
36. Zhang X, Wang JG, Gao F, Ju Y, Liu J (2017) Impact of water and nitrogen fracturing fluids on fracturing initiation pressure and flow pattern in anisotropic shale reservoirs. Comput Geotech 81:59–76
37. Zhang Y, Liu Z, Han B, Zhu S, Zhang X (2022) Numerical study of hydraulic fracture propagation in inherently laminated rocks accounting for bedding plane properties. J Pet Sci Eng 210:109798
38. Zhang Y, Shao J, Liu Z, Shi C (2021) An improved hydromechanical model for particle flow simulation of fractures in saturated rocks. Int J Rock Mech Min Sci 147:104870
39. Zhang Y, Shao J, Liu Z, Shi C, De Saxcé G (2018) Effects of confining pressure and loading path on deformation and strength of cohesive granular materials: a three-dimensional dem analysis. Acta Geotech 14:443–460
40. Zhang Y, Shao J, de Saxcé G, Shi C, Liu Z (2019) Study of deformation and failure in an anisotropic rock with a three-dimensional discrete element model. Int J Rock Mech Min Sci 120:17–28
41. Zhao LY, Shao JF, Zhu QZ (2018) Analysis of localized cracking in quasi-brittle materials with a micro-mechanics based friction-damage approach. J Mech Phys Solids 119:163–187
42. Zhou J, Luqing Z, Zhejun P, Zhenhua H (2016) Numerical investigation of fluid-driven near-borehole fracture propagation in laminated reservoir rock using pfc2d. J Nat Gas Sci Eng 36:719–733
43. Zhu QZ, Kondo D, Shao JF (2008) Micromechanical analysis of coupling between anisotropic damage and friction in quasi brittle materials: role of the homogenization scheme. Int J Solids Struct 45:1385–1405
44. Zisser N, Nover G (2009) Anisotropy of permeability and complex resistivity of tight sandstones subjected to hydrostatic pressure. J Appl Geophys 68:356–370
45. Zoback M, Rummel F, Jung R, Raleigh CB (1977) Laboratory hydraulic fracturing experiments in intact and pre-fractured rock. Int J Rock Mech Min Sci Geomech Abstr 14:49–58

Publisher's Note Springer Nature remains neutral with regard to jurisdictional claims in published maps and institutional affiliations.